Heat Mass Transfer
DOI 10.1007/s00231-015-1731-z

ORIGINAL

Acoustic resonance excitation of turbulent heat transfer and flow reattachment downstream of a fence

Claudio Selcan[1] · Beni Cukurel[1] · Judah Shashank[1]

Received: 21 April 2015 / Accepted: 26 November 2015

Abstract The current work investigates the aero-thermal impact of standing sound waves, excited in a straight channel geometry, on turbulent, separating and reattaching flow over a fence. Effects of distinct frequency resonant forcing ($Re_H = 10{,}050$ and $f = 122$ Hz) are quantified by wall static pressure measurements and detailed convective heat transfer distributions via liquid crystal thermometry. Acoustic boundary conditions are numerically predicted and the computed longitudinal resonance mode shapes are experimentally verified by surface microphone measurements. Findings indicate the presence of a resonant sound field to exert strong influence on local heat transfer downstream of the fence, whereas the boundary layer upstream of the obstacle remains notable unaffected. Upstream shift of the maximum heat transfer location and an earlier pressure recovery indicate a reduction in time averaged flow reattachment length of up to 37 %. Although the streamwise peak Nusselt increased by only 5 %, the heat transfer level in the vicinity of the unexcited reattachment zone was locally enhanced up to 25 %. Despite prominent impact of resonant forcing on the fence wake flow, the total pressure drop penalty remained invariant. Observations demonstrate the significant aero-thermal implications of shear layer excitation by standing sound waves superimposed on the channel flow field.

✉ Beni Cukurel
beni@cukurel.org

Claudio Selcan
selcacfv@technion.ac.il

Judah Shashank
judah@tx.technion.ac.il

[1] Turbomachinery and Heat Transfer Laboratory, Technion-Israel Institute Technology, Technion City, 32000 Haifa, Israel

List of symbols

Roman

c (m/s)	Air speed of sound
D_h (m)	Channel hydraulic diameter
f (Hz)	Sound frequency
f (-)	Darcy friction factor
h (W/m^2 K)	Heat transfer coefficient
H (m)	Fence height
k (W/m K)	Air thermal conductivity
K (1/m)	Wave number
l (m)	Characteristic length scale
LWH (m)	Channel length, width, height
p (Pa)	Pressure
q (W/m^2)	Surface heat flux
Ma (-)	Mach number
Nu (-)	Nusselt number
Re (-)	Reynolds number
SPL (dB)	Sound pressure level
St (-)	Strouhal number
T (K)	Temperature
U (m/s)	Axial velocity
x,y,z (m)	Axial, lateral, vertical direction
Z (Ns/m^3)	Acoustic impedance

Greek

λ (nm)	Sound wavelength
μ (Kg/m s)	Dynamic viscosity
ρ (Kg/m^3)	Air density
ω (Hz)	Angular frequency

Published online: 15 December 2015

Abbreviations

BR	Channel blockage ratio
CW	Clockwise direction
CCW	Counter-clockwise direction
EF	Enhancement factor
FEM	Finite element method
HSI	Hue, saturation, intensity
RGB	Red, green, blue
TC	Thermocouple
TLC	Thermochromic liquid crystal

Subscripts

c	Complex quantity
D	Hydraulic diameter based
H	Fence height based
max	Maximum heat transfer
R	Flow reattachment
∞	Free stream

1 Introduction

Active and passive flow control techniques are commonly employed in a broad range of both laminar and turbulent flow applications, including control of flow transition, boundary layer separation, shear-layer instability alteration and subsequent flow reattachment [1, 2]. A well-established approach involves the introduction of small amplitude periodic disturbances to the flow, where perturbations are induced globally (e.g. acoustic) or locally (synthetic jets, mechanical flaps, plasma actuators) [1]. The common concept underlying these flow control strategies is the deliberate manipulation of downstream shear flow evolution. Flow control over a backward-facing step, owing to its fundamental nature, has received most attention in the research community [3, 4].

1.1 Flow control in a backward facing step

The abrupt volumetric expansion behind a backward-facing step enforces a sudden deceleration of the flow, entailing flow separation and free shear layer formation due to adjacent high velocity freestream and low momentum wake fluid, Fig. 1a. The fluid beneath the separated free shear layer is characterized by a recirculation region, the length of which is confined by the downstream reattachment point, where the shear layer curves downward, impinges on the wall and splits into two fractions [5, 6]. A part of it reattaches to the bounding wall, thus contributing to gradual redevelopment of the ordinary boundary layer [5, 7]. Unable to overcome the adverse pressure gradient imposed by the abrupt cross section expansion, the other part of it is deflected upstream, feeding into the low momentum reversed flow region.

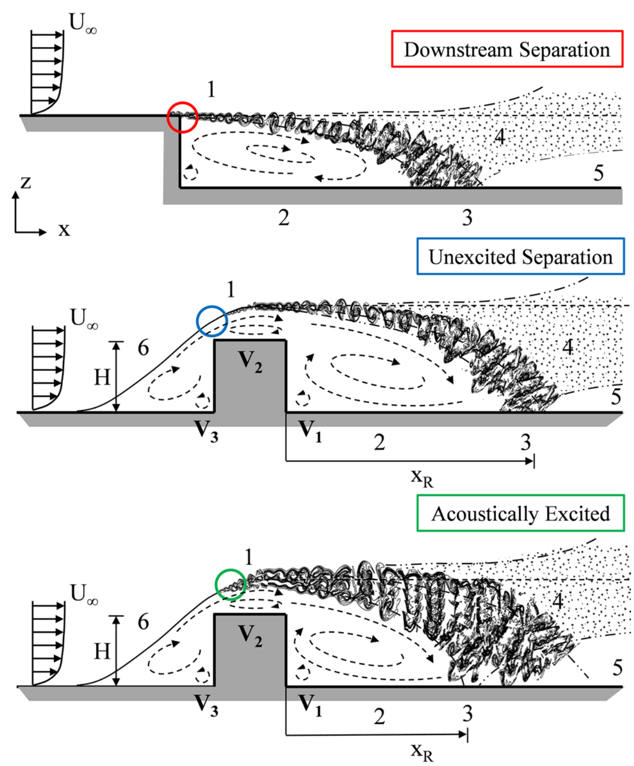

Fig. 1 Step and fence-flow topology: *1* shear layer formation, *2* wake recirculation, *3* reattachment point, *4* shear layer, *5* boundary layer redevelopment, *6* upstream separation

Modification of the separated shear layer and subsequent flow reattachment by periodic forcing has been studied extensively. In backward-facing step flow, harmonic acoustic excitation, below the natural vortex passage frequency (in the step height based Strouhal number range St = 0.1–0.4), was found to be conducive to a notable wake flow alteration [4]. Similarly, a local mechanical excitation at the step edge was demonstrated to have a regularizing effect for the spanwise-correlated structure formation of both laminar and turbulent separating flow [3]. Upstream of the reattachment region, due to forcing-promoted acceleration and vortex structure merging, the spreading rate of the shear layer was increased by higher momentum entrainment [4]. Excitations at the dominant shedding frequency concentrated the formerly distributed turbulent energy into a sharp peak, resulting in the reduction of streamwise reattachment length up to 30 % [3]. Moreover, the spanwise distribution of the reattachment line was observed to be flattened by the periodic excitation, primarily attributed to forcing-induced two-dimensionality of vortical structures in the free shear layer [4, 8]. However, in general, the distinct conducive optimum frequencies in the effective Strouhal range, St=0.1–0.7 remain controversial [3, 4, 9, 10].

As the maximum heat transfer point correlates with the location of an aerodynamic reattachment region [11, 12], a relatively limited number of studies investigated the heat transfer ramifications of reattaching shear layer flow control via periodic disturbances. Employing controlled local forcing at the edge of the backward facing step, the reduced reattachment length was reported to yield increased heat transfer (up to 30 %) in the step wake region for laminar and turbulent flow [13, 14]. Similar observations were made for turbulent separating flow over a flat plate with a squared leading edge, for which a shortened separation bubble along with globally higher heat transfer and augmented maximum heat transfer was reported [15].

1.2 Flow over an isolated fence

Despite similarities in flow topology with a backward facing step, the flow over a fence is of a higher degree of complexity; the oncoming boundary layer state is altered by the rib, reverse flow regions upstream and downstream of the rib are coupled, and the shear layer bounding the wake recirculation bubble is formed at the upstream edge of the fence with an upward angle, Fig. 1b. Furthermore, there exist additional characteristic flow features which include: a CW rotating secondary flow structure in front, a local separated flow region on top, and a CCW rotating vortex at the back face of the rib [16].

Literature pertaining to flow control in ribbed flow geometry is extremely scarce. According to the authors' best knowledge, the only investigation of relevance is purely aerodynamic, where the flow upstream of a high (15 %) blockage ratio fence is excited via local flap and oscillating synthetic jet forcing. In a narrow Strouhal range within St $=$ 0–0.25 a reduction of the turbulent reattachment length by up to 30 % was demonstrated. [17].

1.3 Acoustic resonance effects

Although the beneficial impact of periodic excitation on abruptly separated flow has been shown in several studies, prior investigations have not focused on the impact of acoustic resonances. As traveling waves interact with boundaries, constructive interference of the incident and reflected waves can give rise to spatially-stationary, temporally-oscillating static pressure fields, where sound pressure fluctuations and associated acoustic particle velocity exceed the incident wave amplitude. Standing wave effects on forced convection heat transfer have been demonstrated to be significant particularly for longitudinal resonance modes in attached turbulent duct flow, with local impact depending on Reynolds number and standing wave patterns (node-/antinode locations) [18–20]. Recently, acoustic resonance effects on flow field structures and heat transfer enhancement became of interest for application in thermoacoustic systems and refrigerators [21–24].

1.4 Motivation

The majority of prior literature on separated flow control pertains to local excitation via mechanical devices, delivering a large concentrated and localized energy input. Yet, the implementation of additional miniaturized mechanical components to many geometries (including heat exchange surfaces) is impractical. Addressing this issue, there exists a modest amount of scientific effort addressing the subject of globally excited backward-facing step geometries, however the focus is predominantly on the purely aerodynamic perspective of traveling waves. Extending upon this knowledgebase in abruptly separated flow modulation, the current research investigates convective heat transfer ramifications of resonance excitation (standing sound waves) for flow over an isolated fence. Under a distinct longitudinal standing wave excitation, the aero-thermal implications are contrasted through heat transfer and static pressure distributions across the fence geometry. Towards characterizing the acoustic resonance behavior of the wind tunnel facility and excited mode shape patterns, experimental observations are corroborated by a numerical eigenfrequency analysis.

2 Experimental methodology

2.1 Wind tunnel facility

The experimental wind tunnel facility employed is operated by a centrifugal blower running in aspiration mode; it is decoupled from the test section to damp out mechanical vibrations. Pressure fluctuation propagation from the driving unit is prevented by a settling chamber, equipped with two layers of fine mesh structures. The duct which forms the test and exhaust sections has a 20 $\times$ 20 cm cross section at a length of 4 meters. Upstream, the air is sucked in through a bellmouth inlet of contraction area ratio 25:1, which was designed based on the guidelines proposed in [25]. The inlet is further equipped with a honeycomb and metal screen structure to attain minimum inflow swirl and to diminish spatial non-uniformities.

For setting the aerodynamic operating conditions along the channel, bulk velocity is measured via a Paragon duct mounted airflow measurement station, along with six T-type thermocouples exposed to freestream air at the test

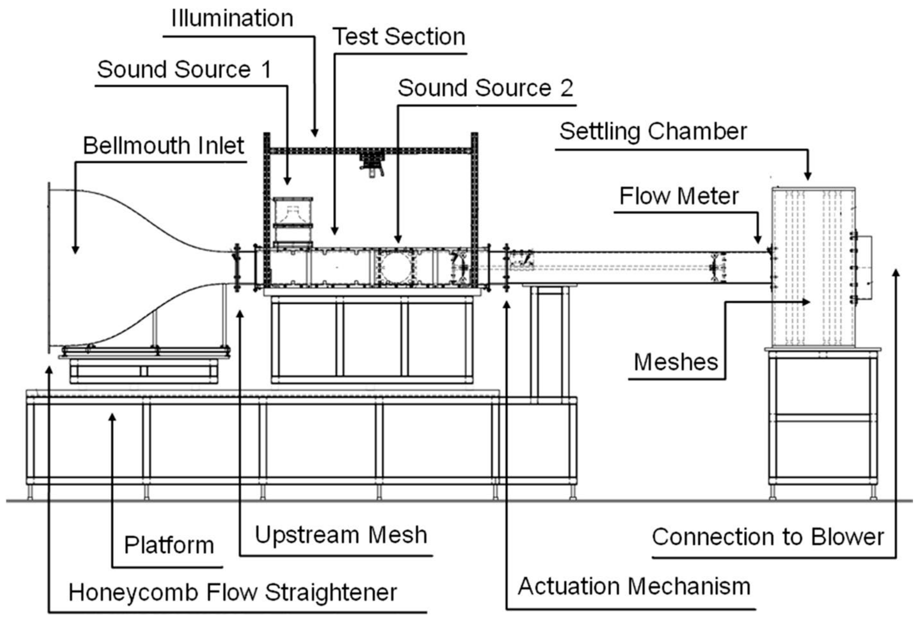

Fig. 2 Schematic of the experimental facility

section inlet and outlet. The facility schematic can be found in Fig. 2.

The test section comprises of 1.5 m long Plexiglas walls which are supported by an aluminum frame. Optical access is enabled from two sides as one wall serves as the heat transfer investigation surface. Situated perpendicular to the mean flow, a single, squared wooden rib element with sharp edges is placed 57 cm downstream of the test section inlet, producing a channel blockage ratio of $H/D_h = 7.5$ %. The steady pressure distributions are acquired by pressure taps located along the channel wall centerline.

A Mackie DLM-8 loudspeaker (zero mass flow) is employed as the active audible frequency range excitation source (65 Hz–20 kHz), placed in a sealed casing on the observation side wall. A squared taut fine steel wire mesh (25 µm cell size), covering the entire 20 cm duct height, allows for the acoustic excitations to permeate within the test section with minimal distortion of the channel flow, Fig. 3. Acoustic boundary conditions are acquired by a high-sensitivity wide frequency range (4 Hz–70 kHz) pressure field condenser microphone (type *G.R.A.S. 46BD)*, flush mounted to the heat transfer surface side wall at the centerline. The signal is amplified with an *Endevco Meggitt Model 133* conditioner, followed by acquisition via *National Instruments NI 9205* module at 200 kS/s sampling rate, and subsequent Fast Fourier Transform spectral analysis.

2.2 Acoustic resonance modes

To study the impact of longitudinal standing waves, the test section is bounded by two fine steel wire meshes (25 µm cell size with 60 % blockage ratio) which confine the upstream and downstream ends of the test section. The mesh structures modify the acoustic boundary conditions by partial wave reflection and encourage formation of a cuboid closed duct cavity, mimicking the behavior of a resonance tube. Assuming a cuboid space of acoustically hard walls and length L, width W and height H, Fig. 3, the resonance frequencies are estimated in a first approximation according to:

$$f_{l,m,n} = \frac{c}{2} \cdot \left[1 - \left(\frac{U_\infty}{c}\right)^2\right]^{1/2} \cdot \sqrt{\left(\frac{l}{L}\right)^2 + \left(\frac{m}{W}\right)^2 + \left(\frac{n}{H}\right)^2} \quad (1)$$

where $l, m, n = 0, 1, 2$ denotes the higher harmonics [26].

2.3 Liquid crystal thermometry

Measurement of time-averaged convective heat transfer is conducted by means of wide-band liquid crystal thermometry at steady state. This allows optical acquisition of high-resolution spatial distributions of surface temperature and heat transfer coefficient. Cholesteric micro-encapsulated TLCs, type R35C20W by Hallcrest Inc., are employed. A spatially-uniform constant-heat flux thermal boundary condition is implemented by a 25 µm thick Inconel foil which is attached to the vertical heat transfer measurement surface. Covering the entire axial length and 90 % (18 cm out of 20 cm) of the channel height, the test plate is subjected to Joule heating from an *Agilent 6032A* DC power supply. The imposed surface heat flux q is calculated from supplied voltage and current $q = V \cdot I$.

For optimal TLC color-play brilliance and contrast, the thermochromic liquid crystals are deposited on a uniform underlying layer of matte black paint which exhibits a

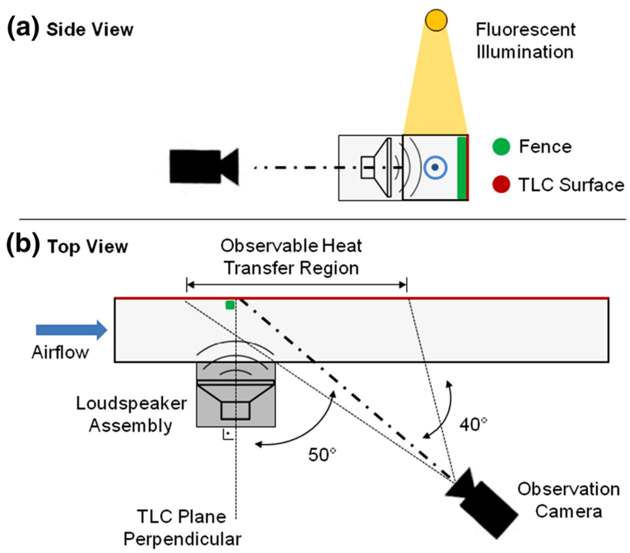

Fig. 3 Illustration of the experimental configuration

non-dazzling surface due to diffuse reflection. The test surface TLC response is observed via a Nikon D300S digital camera, placed at a 20° observation angle from the channel axis. A camera off-axis illumination configuration is used, ensuring minimum surface reflections, shadows and overcoming issues of non-uniformity.

Illumination is provided by OSRAM type T8 L 36W fluorescent lights, mounted above the principal axis, irradiating at a 1 m vertical distance from the TLC surface, Fig. 3. The entire test section and observation camera are covered with a thick black cloth to prevent spurious background illumination sources.

2.4 TLC calibration and data reduction

During data acquisition, high-resolution images of the active TLC surface are captured in the RGB color space of the camera. To reduce a possible angular dependency due to camera-lighting off-axis arrangement, a background subtraction routine is utilized. RGB values of the unheated/inactivated TLC surface (background image) are sampled at the beginning of an experiment and subtracted from every subsequent measurement image. The effectiveness of this methodology was previously demonstrated [27].

In order to quantify the local surface temperature, RGB tristimulus color values are mapped into the HSI space:

$$H = 1/2\pi \cdot \tan^{-1}\left[\sqrt{3} \cdot (G - B)/(2R - G - B)\right] \quad (2)$$

The hue-angle color quantity can be uniquely correlated to temperature by a monotonously increasing, single valued and continuous function. This enables the unambiguous calculation of local surface temperature from the camera-recorded TLC response.

Hue-temperature calibration curve is established by an in-situ calibration at natural convection, using 4 T-type surface thermocouples located at the downstream end of the test plate. Arranged in a cross shaped configuration and enclosing a small TLC coated square (1 cm × 1 cm), the hue-angle value of exposed area is acquired and correlated with averaged thermocouple readings. The successively imposed temperature levels span the entire TLC color play bandwidth. Discrete data is fitted by a twice-differentiable, monotonically increasing 20 knot cubic spline. Details of TLC thermometry technique and the calibration procedure are given in [27].

Due to the inclined observation path, sampled images are subject to significant perspective distortions. Each region of the image must therefore be mapped and projected separately onto a single plane via independent bicubic transformation, Fig. 4. Accordingly, due to the optical path, the magnification factor varies along the test plane; as an overall indicator, the averaged mean scale factor is calculated to be 12 pixels/mm.

Finally, after utilizing the calibration curves and converting acquired hue-angle distributions to the desired maps of surface temperatures, the raw temperature data is subjected to a series of median and Gaussian low pass filters.

2.4.1 Enhancement factor calculation

The local convective heat transfer coefficient is calculated from the (conduction losses-corrected) Inconel heat flux, the TLC-acquired surface temperature and the bulk temperature along the channel axis (linearly approximated from the inlet and exit section TC measurements):

$$h(x, y) = q/(T(x, y) - T_\infty(x)) \quad (3)$$

which is further non-dimensionalized by the channel hydraulic diameter based Nusselt Number:

$$Nu_D(x, y) = h(x, y) \cdot D_h/k_{air} \quad (4)$$

Sound-induced modification of convective heat transfer is quantified by the local enhancement factor EF, contrasting the Nusselt number in the presence and the absence of forcing:

$$EF = Nu_{excited}/Nu_{unexcited} \quad (5)$$

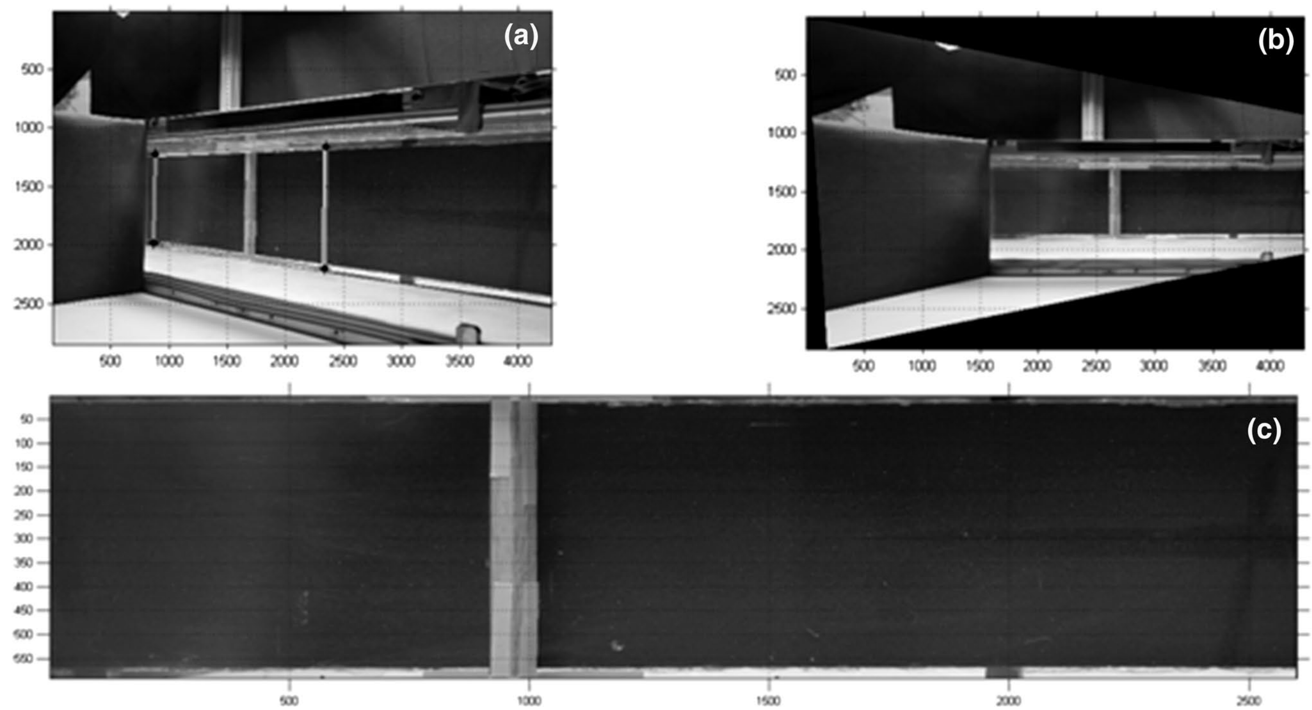

Fig. 4 Image perspective correction: **a** raw form, **b** projective transformation, **c** cropping

2.5 Uncertainty analysis

The measurement uncertainty is estimated according to the single sample method proposed in Ref. [28]. The overall uncertainty in wall temperature is determined by the uncertainty of thermocouple readings (±0.35 K), hue-angle contribution of the fixed broadband image noise (±0.25 K), the liquid crystals' angular dependency (±0.3 K) and deviation from the hue-temperature curve fit formulation (±0.2 K). This results in a combined wall temperature uncertainty of (±0.55 K). The major contributor to the heat flux uncertainty is the back face conduction loss, which yields deviations up to ±2.4 %. Along with uncertainty on flow temperature, air thermal conductivity and hydraulic diameter measurement, the resulting nominal Nusselt number error is ±3.6 %. The error associated with the enhancement factor, however, is a matter of measurement precision, and not necessarily accuracy. As a consequence, the EF uncertainty is determined in terms of repeatability and is estimated to be less than ±1.5 %.

The total uncertainty in Reynolds number is in the order of 3.5 %. This value represents an upper bound on measurement accuracy, as the experimentally determined mean deviation (precision) appears to be around 0.5 %, adequate to ensure satisfactory repeatability.

3 Numerical simulation

3.1 Technical approach

In order to accurately predict complex modal characteristics and natural frequencies of the experimental test rig, a numerical simulation is carried out using COMSOL Multiphysics [29]. By assuming rigid boundary conditions for the passage enclosure and considering low mean flow Mach number ($Ma \ll 0.1$), the numerical domain is modeled by the Acoustic module, where sound-structural and aero-acoustic coupling is neglected. The FEM-modeled 3D geometry includes every air cavity component of the test facility: upstream bellmouth inlet, squared test section duct, downstream settling chamber as well as the compressor plenum and air outlet duct.

An unstructured mesh of 668,100 s-order Lagrange tetrahedral elements (971,000 degrees of freedom) is used to solve the sound pressure field in the Helmholtz equation, Eq. 6, in the frequency domain. This describes sound propagation in a gaseous medium at time-harmonic pressure fluctuations. The formulation of the problem (absent of source terms) can be written as,

Table 1 Numerical simulation boundary conditions

Wall enclosure			Acoustically hard (rigid) wall
Inlet			Plane wave radiation
			Incident pressure wave (1 Pa)
Outlet			Plane wave radiation
Mesh-, screen inserts	Interior perforated plate		
	Turbulence mesh	Honeycomb	Metal screens
Area porosity σ (–)	0.1	0.75	0.6
Hole diameter d_h (m)	25×10^{-6}	0.010	0.001
Plate thickness t_p (m)	0.0001	0.2	0.0007
End correction δ_h	0.25 d_h	0.25 d_h	0.25 d_h
Flow resistance θ_f	–	–	–

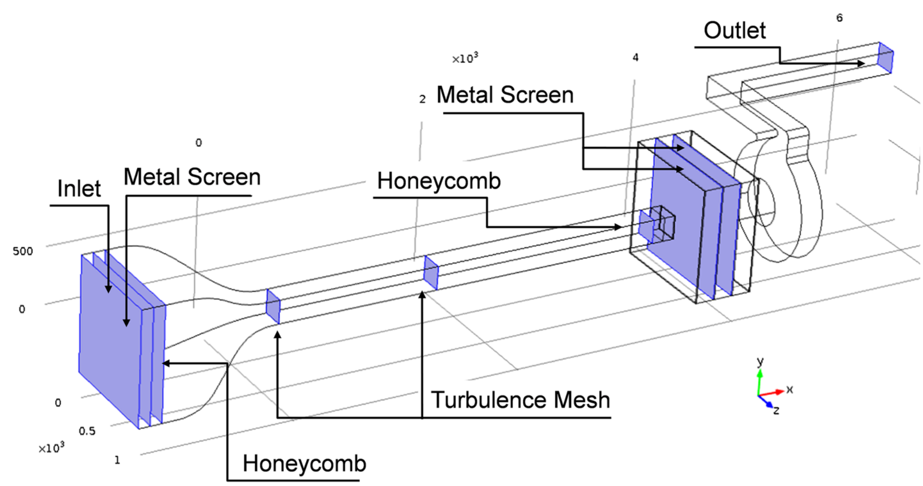

Fig. 5 Computational domain boundary conditions

$$\nabla \cdot \left(-\frac{1}{\rho} (\nabla p) \right) - \frac{\omega^2 p}{\rho c^2} = 0 \tag{6}$$

where $\omega = 2\pi f$ is angular frequency, ρ is the fluid density, and c is the speed of sound. Sound wave attenuation due to viscous dissipation and thermal effects (bulk fluid viscosity/-thermal conduction and acoustic boundary layer absorption) are not modelled. For appropriate resolution of the sound waves, the mesh element size (max 40 mm) is set to be <1/6th of the minimum wavelength of interest, $\lambda_{min} = 2.01$ m. Furthermore, the degrees of freedom (DOF) associated with the discrete mesh has been adjusted by the number of cells to meet the criterion for adequate wave resolution in the direction of propagation, $DOF_{min} = 1728 \cdot V/\lambda_{min}^3$ [29]. A Grid independency study has been carried out, and further mesh refinement does not indicate significant changes.

The simulation is conducted using the boundary conditions listed in Table 1: while rigid walls (sound hard boundary condition) are assumed for the enclosure, plane wave radiation is set at inlet and outlet sections, Fig. 5. Honeycomb, turbulence-meshes and screen inserts are modeled as interior perforated plates: as the Mach number is small (Ma ≪ 0.1), convective effects and flow resistance θ_f across plate boundaries are omitted. Acoustic transfer impedances Z are calculated according to the model expression [29, 30]:

$$\frac{Z}{\rho_c c_c} = \left(\frac{1}{\sigma} \sqrt{\frac{8\mu K}{\rho_c c_c}} \left(1 + \frac{t_p}{d_h} \right) + \theta_f \right) + i \frac{K}{\sigma} \left(t_p + \delta_h \right) \tag{7}$$

Visualization of the associated eigenmodes localizes the regions which host the resonance effect, and allows for the identification of frequencies that entail local influence on the test surface.

3.2 Acoustic resonance analysis

The response of the facility to sound forcing is analyzed in the 100–200 Hz frequency range. The relevant acoustic eigenmodes (123, 167 Hz) are illustrated by distributions of the total acoustic pressure in Figs. 6 and 7. Evidently, for 123 Hz, a characteristic standing wave pattern occupies the straight duct section, Fig. 6. On the other hand, the resonance mode predicted at 168 Hz exhibits a coupled

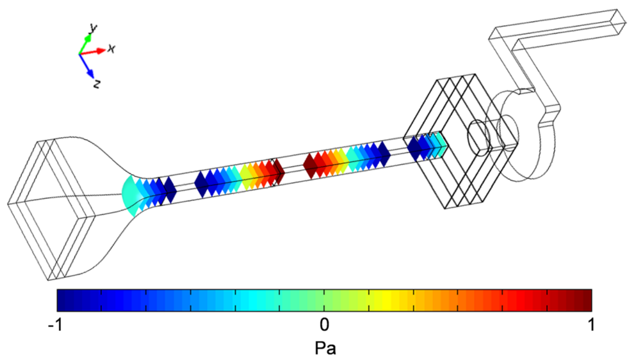

Fig. 6 Total acoustic pressure at 123 Hz excitation

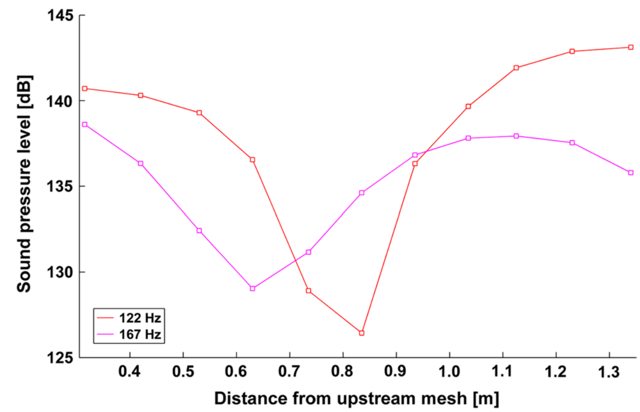

Fig. 8 Sound-pressure-level variation inside the test section

behavior between the bellmouth inlet, and the cuboid section, Fig. 7. Hence, the numerical results indicate sound forcing at both eigenfrequencies 123 and 167 Hz to exert strong direct influence on the measurement surface due to excited longitudinal acoustic resonance modes of the duct.

Numerically predicted resonances of the wind tunnel are validated via unsteady pressure measurements along the channel wall center-plane, spanning a distance of 30 to 135 cm downstream of the inlet mesh. The sound pressure level distributions at two different excitation frequencies (122 and 167 Hz), are charted in Fig. 8. The spatial variation and apparent node/antinode behavior is indicative of characteristic longitudinal standing wave patterns inside the test section. In agreement with associated numerical predictions, the sound pressure node of 122 Hz is seen to be induced at around 0.8 m, while corresponding antinodes are located further upstream and downstream by 0.5 m. Similarly, close agreement between experimental and numerical results is observed in the case of 167 Hz excitation. The longitudinal mode shape pattern is shifted and the associated pressure node is situated 0.2 m ahead of the 122 Hz resonance node, thus closer to the rib obstacle located at 0.57 m.

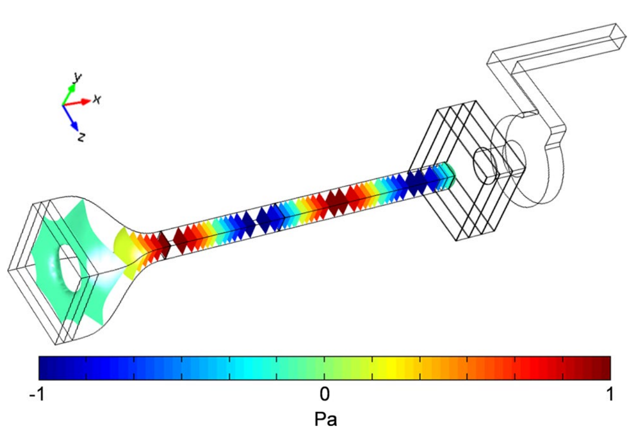

Fig. 7 Total acoustic pressure at 167 Hz excitation

Moreover, depending upon the location throughout the test section, the standing sound wave-induced SPL for 122 and 167 Hz excitations are of similar magnitude. In both resonance excitation cases, the rib-roughened flow is subjected to the strong direct influence of periodic localized acoustic pressure/velocity fluctuations.

4 Experimental results

Measurements of steady and unsteady pressure, as well as convective heat transfer experiments, are conducted for a nominal Reynolds number of $RE_D = 134{,}000$ and $RE_H = 10{,}050$, based on channel hydraulic diameter (20 cm) and rib height (1.5 cm) respectively. The rib aspect ratio ($D_h/H = 13.3$), >10, satisfies the two-dimensionality criterion of reattaching flows, defined for rearward-facing steps [31]. Therefore, the flow at the symmetry plane is assumed to be unaffected by lateral wall influence. The acoustically excited flow is subjected to harmonic forcing at 120 Hz (corresponding to a, step height based, Strouhal number $St = f \cdot H/U = 0.17$) at 131 dB SPL. In comparison, for mean flow velocities up to 10 m/s, the background noise is measured to be <80 dB absent of excitation.

4.1 Baseline heat transfer distribution

For a region spanning 30 to 108 cm from inlet mesh, the unexcited baseline heat transfer distributions are portrayed in terms of the Nusselt number (Nu_D); referenced with respect to the fence downstream edge, this corresponds to $-20 < x/H < -32$, Fig. 9. As no heat transfer data is acquired on top and directly upstream of the rib (due to the blocked camera observation path), regions $-2.33 < x/H < 0$ are blanked out. The line of streamwise maximum in heat

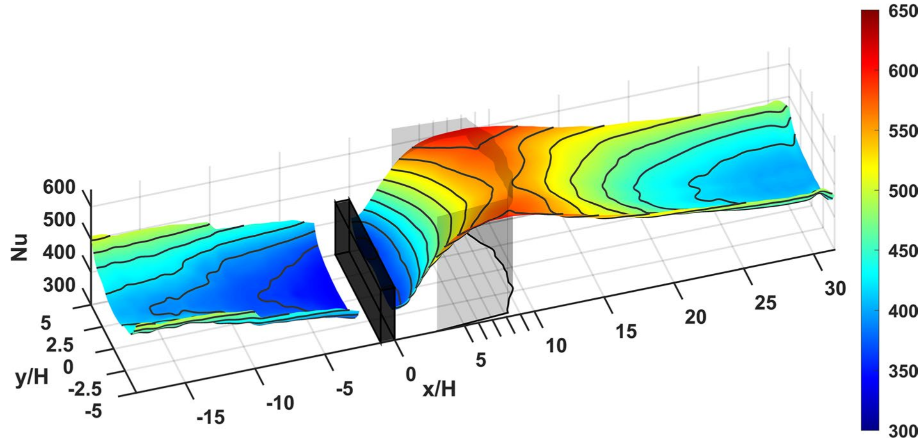

Fig. 9 Baseline unexcited Nusselt distribution

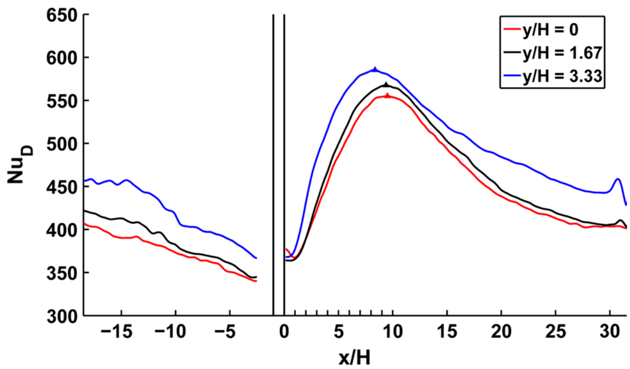

Fig. 10 Baseline unexcited streamwise Nusselt development

transfer, x_{max}, is indicated by the thin grey line. To further illustrate the streamwise Nu_D trends, line charts are presented at three lateral planes, located at channel symmetry line and two other points towards the side wall, corresponding to y/H = 0; 1.67; 3.33, Fig. 10. An asterisk indicates the point of local maximum in heat transfer for each plane.

The characteristic aero-thermal features of the rib-roughened flow topology were previously discussed in detail for high blockage ratios (BR = 30 %) and similar Reynolds number Re_H = 12,000 [16, 32, 33]. Examining the current Nu_D findings (for BR = 7.5 % at Re_H = 10,050), Fig. 9, the upstream region $-19 < x/H < -2.33$ is characterized by the unperturbed boundary layer development over a flat plate prior to the influence of the rib obstacle. In this state, an overall gradual decrease in heat transfer is associated with boundary layer thickening at increasing development length from the inlet, Fig. 10. Overall, towards the lateral wall y/H ~ 3.3, higher levels of heat transfer are observed, as a result of the corner wall vortices associated with the channel flow geometry.

Approaching the rib, due to the potential blockage effect, the flow separates from the surface and deviates around the rib obstacle. Owing to reduced cross-sectional area, it is locally accelerated and subsequently experiences an abrupt step change at the backward face of the rib. Confined by the flow reattachment line, an elongated recirculation bubble is formed. In current configuration, the separated flow region occupies a distance of approximately 8–10 H.

As the most prominent flow feature, the flow reversal exerts large variations in heat transfer; in addition to forming a low momentum region, the entrainment of cool free stream fluid is prevented. Thus, as observed in Figs. 9 and 10, the rib wake separation bubble imparts a global minimum in Nusselt number $Nu_D = 370$ at the immediate vicinity of the rib (x/H ~ 0), which is evident along the entire passage width.

Further downstream of the rib from x/H ~ 1.5, the Nusselt number begins to increase monotonously, as a consequence of the diminishing rib wake effects which allow cooler flow to be progressively entrained from the mainstream. At an increased axial position, this steep rise reaches a global maximum (Nu_D ~ 580) in the vicinity of the reattachment point. This is associated with the strong impingement of the separated free shear layer on the bounding wall, subjecting the heated surface to low-temperature, high-momentum fluid.

Although the aerodynamic reattachment point (x_R) and maximum streamwise heat transfer position (x_{max}) do not universally coincide for all separated flows, x_{max} is considered as the relevant indicator of skin friction reversal point [5, 12]. Towards the sidewalls, the local heat transfer maxima levels increase, the positions of which are observed slightly further upstream, Fig. 9. This curved spanwise distribution and laterally increasing heat transfer are attributed to the aerodynamic wall effects and rolled up corner vortices being advected over the rib from the upstream separation point [13, 16]. Beyond the reattachment point, x/H > 10, the heat transfer decreases monotonically in the streamwise direction with the redeveloping thermal boundary layer and eventually re-approaches its initial unperturbed boundary layer state, x/H > 27.

Fig. 11 120 Hz excited Nusselt number distribution

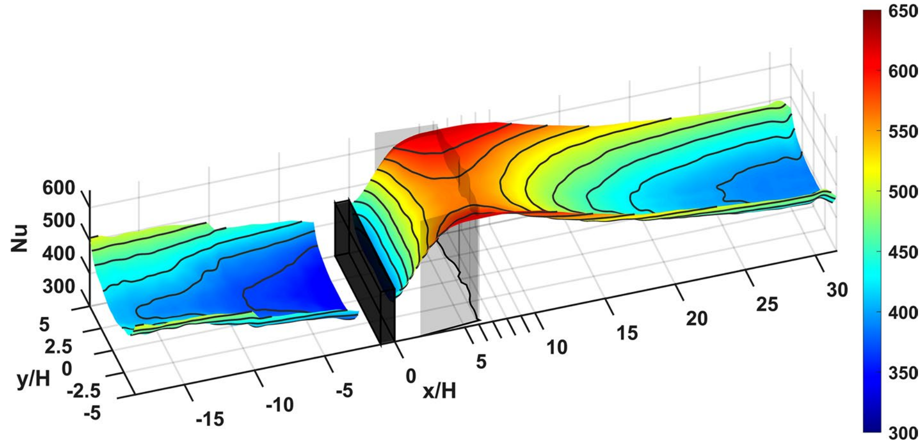

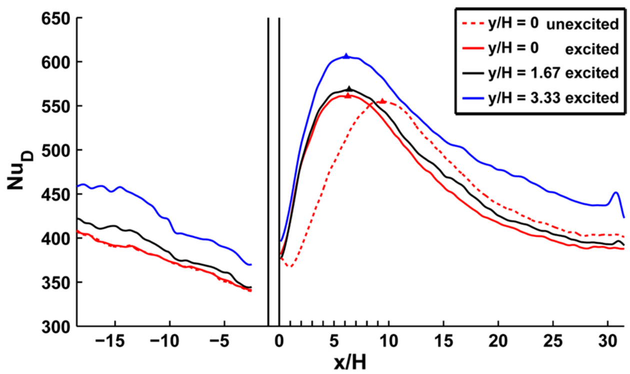

Fig. 12 120 Hz *centerline* Nusselt number comparison

4.2 Excitation effects on heat transfer

In order to investigate the heat transfer implications of sound excitation, the flow over a fence is subjected to acoustic resonance forcing at 120 Hz with a 131 dB source amplitude. The resulting distributions of Nusselt number are displayed in Fig. 11, and the longitudinal Nu_D variation at three lateral positions are charted in Fig. 12. Comparing these results to the unexcited case in Fig. 9, the forcing induced heat transfer is significantly affected by acoustic perturbations, Fig. 11—albeit retaining an overall self-similar pattern. To highlight this impact, Fig. 12 features the unexcited Nusselt number trend at the centerline position.

Regions upstream of the rib ($x/H < 2.33$), which feature flat plate boundary layer development, appear to be impervious to acoustic excitation, Figs. 11 and 12. On the contrary, downstream of the step disturbance and around the reattachment region, $0 < x/H < 15$, the sound forcing has a significant effect on the local flow field and the associated heat transfer distribution, Fig. 11. While the local minimum remains fixed at the rib back face ($x/H = 0$), the steep streamwise gradient of heat transfer in the separation region appears to be augmented as a consequence of the sound excitation, Fig. 12. A small increase in the peak heat transfer level is observed. The extent of the recirculation bubble is significantly reduced under the influence of acoustic excitation, shifting the location of centerline maximum heat transfer from $x_{max}/H = 9.5$ to $x_{max}/H = 6$. Towards the lateral walls at $y/H \geq 3.33$, a similar observation can be made, moving x_{max}/H from 8.5 to 6, Fig. 11. Therefore, while the line of unexcited flow reattachment exhibits a curved shape in the spanwise direction (Fig. 9), it becomes flattened in the presence of forcing—evidenced by uniform $x_{max}/H = 6$ in Fig. 11. Under different experimental conditions, excitation is demonstrated to lower flow three-dimensionality at the location of shear layer impingement [4, 13]. Further downstream, as the excited thermal boundary layer starts to develop at an earlier streamwise position, the local heat transfer level at re-attached flow condition appears to be lower with respect to the unexcited case.

Illustrating the localized sound alteration of heat transfer, Fig. 13 presents the enhancement factor, ratio of the excited to unexcited Nusselt numbers. Upstream of the rib, indicated by uniform EF ~ 1, the effect of acoustic excitation is notably absent. There is an upstream shift of the bell shaped Nusselt curve in the immediate wake of the fence, Fig. 12. Therefore, pronounced heat transfer augmentation is observed at $x/H = 0$–8 over the entire span of the channel. With a maximum around the centerline at $x/H \sim 1.5$ and $|y/H| < 2.5$, enhancement factor exhibits an increase up to 25 %. This alteration is not as prominent towards the lateral side walls.

Further downstream, the heat transfer enhancement decreases gradually. Decaying to unity slightly upstream of the unexcited reattachment point ($x/H = 8$), it reaches a global minimum at $x/H = 12.5$. Far away from the obstacle, with the EF re-approaching unity, the sound induced effects gradually diminish. Averaging the Nusselt number in the lateral and streamwise directions within the excited separation region ($0 < x/H < 6.33$ and $-5 < y/H < 5$), the integral heat transfer is augmented by 15 %. If the

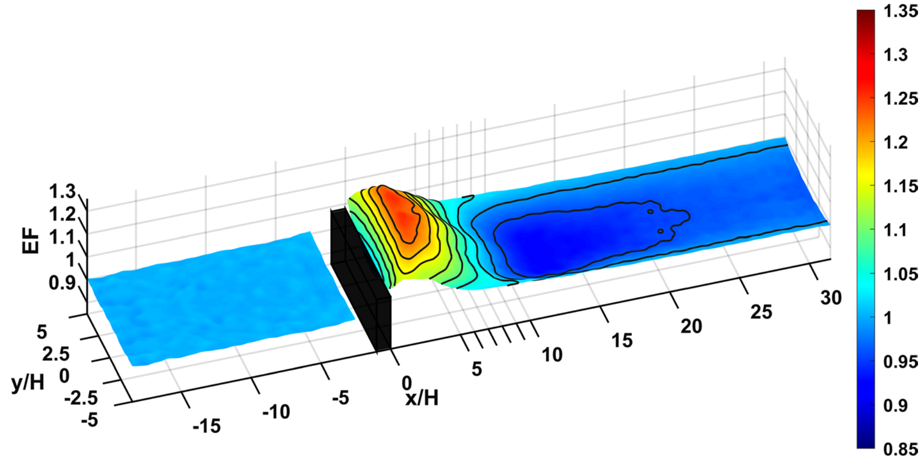

Fig. 13 120 Hz excitation enhancement factor

control surface is extended to the unexcited separation region (0 < x/H < 6.33 and −5 < y/H < 5), a net global increase of 10 % is observed. If the area of interest is much larger, 0 < x/H < 25 and −5 < y/H < 5, the average gain is limited to 2 %; and with larger surfaces, it asymptotically abates to zero.

4.3 Excitation effects on static pressure

From a complementary aerodynamic perspective, in order to assess the implications of a local pressure drop by acoustic forcing in the fence wake, prior heat transfer measurements are supplemented by static wall pressure data. Absent and present of 120 Hz excitation, Fig. 14 presents the pressure development along the channel centerline over a distance of 30 rib heights around the rib. Reported in reference to the fence upstream port at x/H = −10, the values are normalized by the dynamic pressure head: $(p-p_{ref})/(0.5\rho U^2)$.

As the flow encounters the perturbator, $-8 > x/H > -1$, the initially streamwise constant static pressure rises due to the potential blockage effect, which is typical for the mean flow topology in the presence of an obstacle, Fig. 1b. Furthermore, consistent with prior findings for heat transfer, the acoustic excitation does not impose any changes to the local pressure field, supporting the observation that the oncoming upstream boundary layer is unaffected by acoustic forcing, Fig. 14. Furthermore, it is clear that heat transfer is not a function of pressure distribution, but is rather, influenced by flow structures. In contrast, notable excitation induced effects are apparent in the region downstream of the fence, $0 < x/H < 13.5$

For the baseline case absent of forcing, the wall pressure in the separation region initially reduces in the streamwise direction and reaches a global minimum at x/H = 3. Thereafter, the static pressure exhibits a gradual rise with constant slope until a region past the reattachment point,

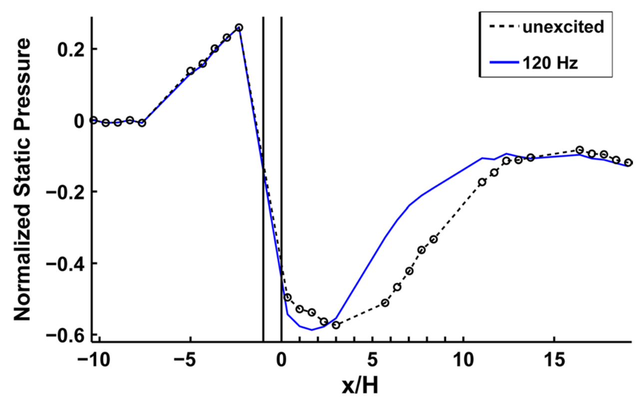

Fig. 14 *Centerline* static pressure development

x/H = 12.5. Further downstream, the curve maintains a constant level in the redeveloping flat plate boundary layer. In the presence of the excitation, although the general trends are retained, there seems to be a greater pressure drop at the immediate vicinity of the rib, followed by an earlier minimum at x/H = 1.5. Subsequently, evidenced by the initially steeper rise in static pressure signature, an earlier recovery is observed; downstream of the excited maximum heat transfer point ($x_{max}/H = 6$) this slope diminishes. Remarkably, the same plateau of downstream static pressure level is reached at around an identical location of x/H = 12.5. Independent of excitation state, the integral pressure drop penalty incurred by the flow over the fence obstacle is characterized by the Darcy friction factor of around $f = 014$. Therefore, the total pressure loss is inferred to remain constant.

5 Discussion

Based on the premise of convective heat transfer in the vicinity of turbulent separating and reattaching flow over a fence obstacle to be affected by sound excitation, the current work investigates ramifications of acoustic resonance forcing on heat transfer distributions and flow reattachment by detailed liquid crystal thermometry. Towards contributing to the understanding of this complex physical phenomenon, numerical prediction is to pinpoint experimental conditions conducive to standing wave excitation, hence to define acoustic boundary conditions that potentially entail aero-thermal modulation.

In the first step of this work, the numerical part is limited to identification of eigenfrequencies and mode shapes. Acoustic boundary conditions towards shear layer and flow structure modulation are modeled by a FEM simulation of the sound field in a generic straight passage geometry. The level of reduction employed in the numerical approach captures all the relevant physical aspects associated with the resonance creation mechanism. Eigenfrequencies and resulting mode shape patterns are predicted by a simple analytical model and further reproduced numerically, providing accurate information on the sound field. Subsequently, numerical predictions are experimentally corroborated for the wind tunnel facility resonance case by flush mounted microphone measurements: computed eigen frequencies and modes (location of the pressure anti-node) are demonstrated to conform with the experimental SPL distributions. In the following second step, ramifications of identified acoustic resonance excitation on heat transfer and flow reattachment are determined by Nusselt number distributions via steady wide-band liquid crystal thermometry.

While this work revealed the pronounced heat transfer impact of acoustic resonances on the reattaching rib flow, it still ambiguous whether forcing effectiveness is determined by the presence of a fixed eigenfrequency acoustic resonance mode, or whether it is the result of standing wave excitation in a favorable Strouhal regime. Future work on the subject should include the effectiveness of standing and travelling sound wave excitations via a parametric frequency (Strouhal number) and amplitude variation.

Most research effort in literature on separating and reattaching shear flow over backward-facing steps and fence geometries devote attention to traveling sound wave excitation. In contrast, standing sound wave (acoustic resonance) impact has only been studied in wall-bounded (attached) flows in straight ducts and pipes, absent of free-shear layers. Therefore, conditions created in the current combined numerical and experimental investigation, by highlighting the implications of standing sound waves on aero-thermal separating and reattaching shear flow over a fence, are to provide novel physical insight on a fundamental phenomenon relevant to the research community.

6 Conclusion

Within the scope of this article, effects of acoustic resonances on turbulent convective heat transfer and separated flow reattachment were studied in the presence of a squared fence obstacle of 7.5 % passage blockage ratio at a channel Reynolds number of 134,000. A longitudinal standing sound wave was excited by an acoustic forcing at 120 Hz (St = 0.17) with a source SPL of 131 dB. The corresponding resonance mode shape patterns of the wind tunnel facility were predicted by a numerical simulation and verified experimentally through surface microphone measurements.

Regions upstream of the rib feature flat plate boundary layer development and appear to be impervious to acoustic excitation despite the elevated SPL. This was evidenced by heat transfer and wall static pressure measurements. On the contrary, a pronounced impact on the rib downstream separation region was ascertained. A strong diminishing influence on the recirculation bubble was manifested as an upstream shift of the maximum heat transfer line by up to $\Delta x_{max} = 3.5H$ or 37 %. Similarly, but for mere traveling wave excitations, the literature results indicated a 30 % reduction in aerodynamic reattachment length [3]. This was most prominent at the channel centerline. Therefore, exhibiting a curved shape absent of forcing, the flow reattachment line under excitation flattened significantly in the lateral direction. Retaining an overall self-similar pattern, the streamwise bell shaped Nusselt curve moved upstream with a slight increase in maximum heat transfer of 5 %, in general agreement with numerical predictions on sound excited flow over a backward-facing step absent of resonance [14]. Yet, the heat transfer distribution prior to the unexcited reattachment point was locally enhanced up to 25 %, while a slight reduction of 8 % was observed further downstream.

Complementary measurements of the wall static pressure clearly reflected the upstream shift of the time-averaged reattachment region, where a steeper local static pressure recovery was observed. Similar aerodynamic observations were reported for an oscillating jet upstream of a fence [17]. However, further downstream, the static pressure level stayed invariant, such that the integral pressure drop penalty associated with the rib flow remained entirely unchanged by the sound forcing. Thence, the associated aerodynamic loss mechanism was inferred to be unaffected despite prominent excitation induced changes in the reattachment region.

In conclusion, acoustic resonance at a single frequency was demonstrated to have beneficial implications on heat transfer and flow reattachment, without an added pressure drop penalty.

Acknowledgments The authors acknowledge the financial support of Technion-IIT, Minerva Research Center (Max Planck Society Contract AZ5746940764), Israel Science Foundation (Individual Grant No. 1752/15) and L. Kraus Research Fund towards initialization of this work. Furthermore, the scholarships which are utilized towards accommodation of Mr. Claudio Selcan in Israel, provided by the Heinrich Hertz-Stiftung (Ministry of Innovation, Science and Research of North Rhine-Westphalia), and Erich Becker-Stiftung (Fraport AG), are greatly appreciated.

References

1. Rice EJ, Zaman KBMQ (1987) Control of shear flows by artificial excitation, in NASA technical memorandum. NASA, Cleveland
2. Greenblatt D, Wygnanski IJ (2000) The control of flow separation by periodic excitation. Prog Aerosp Sci 36:487–545
3. Roos FW, Kegelman JT (1986) Control of coherent structures in reattaching laminar and turbulent shear layers. AIAA J 24(12):1956–1963
4. Bhattacharjee S, Scheelke B, Troutt TR (1986) Modification of vortex interactions in a reattaching separated flow. AIAA J 24(4):623–629
5. Zukauskas VA, Pedisius KA (1987) Heat transfer to reattached fluid flow downstream of a fence. Wärme- und Stoffübertrag 21:125–131
6. Eaton JK, Johnston JP (1981) A review of research on subsonic turbulent flow reattachment. AIAA J 19(9):1093–1100
7. Bradshaw P, Wong FYF (1972) The reattachment and relaxation of a turbulent shear layer. J Fluid Mech 52(1):113–135
8. Kang SG et al (2000) Heat transfer characteristics in separated flows controlled by acoustic excitation. JSME Int J 43(4):653–658
9. Chun KB, Sung HJ (1998) Visualization of a locally-forced separated flow over a backward-facing step. Exp Fluids 25:417–426
10. Roshko A, Sigurdson LW (1985) Controlled unsteady excitation of a reattaching flow. In: American institute of aeronautics and astronautics, shear Flow control conference, vol 1. Boulder, CO, pp 12–14
11. Vogel JC, Eaton JK (1985) Combined heat transfer and fluid dynamic measurements downstream of a backward-facing step. ASME J Heat Transf 107:922–929
12. Sparrow EM, Kang SS, Chuck W (1987) Relation between the points of flow reattachment and maximum heat transfer for regions of flow separation. Int J Heat Mass Transf 30(7):1237–1246
13. Inaoka K, Kakamura K, Senda M (2004) Heat transfer control of a backward-facing step flow in a duct by means of miniature electromagnetic actuators. Int J Heat Fluid Flow 25:711–720
14. Mehrez Z et al (2009) The influence of the periodic disturbance on the local heat transfer in separated and reattached flow. Heat Mass Transf 46(1):107–112
15. Cooper PI, Sheridan JC, Flood GJ (1986) The effects of sound on forced convection over a flat plate. Int J Heat Fluid Flow 7(1):61–68
16. Casarsa L, Arts T (2005) Experimental investigation of the aerothermal performance of a high blockage rib-roughened cooling channel. ASME J Turbomach 127(3):580–588
17. Siller H, Fernholz H-H (2007) Manipulation of the reverse-flow region downstream of a fence by spanwise vortices. Eur J Mech -B/Fluids 26(2):236–257
18. Purdy KR, Jackson TW, Gorton CW (1964) Viscous fluid flow under the influence of a resonant acoustic field. ASME J of Heat Transf 86:97–106
19. Purdy KR et al (1965) The effect of a resonant acoustic field on laminar flow in a circular tube, in ARL Report No. ARL65-96
20. Jackson TW et al (1965) Investigations of the effect of acoustic vibrations on convective heat transfer, in ARL Report No. ARL-65-97
21. Berson A, Michard M, Blanc-Benon P (2008) Measurement of acoustic velocity in the stack of a thermoacoustic rrefrigerator using particle image velocimetry. Heat Mass Transf 44(8):1015–1023
22. Wetzel H, Herman C (1999) Experimental study of thermoacoustic effects on a single plate part II: heat transfer. Heat Mass Transf 35(6):433–441
23. Wetzel H, Herman C (2000) Experimental study of thermoacoustic effects on a single plate part I: temperature fields. Heat Mass Transf 36(1):7–20
24. Wantha C, Assawamartbunlue K (2013) Experimental investigation of the effects of driver housing and resonance tube on the temperature difference across a thermoacoustic stack. Heat Mass Transf 49(6):887–896
25. Bell JH, Mehta RD (1988) Contraction design for small low-speed wind tunnels. August 1988
26. Morse PM, Ingard KU (1968) Theoretical acoustics. McGraw-Hill, New York
27. Cukurel B, Selcan C, Arts T (2012) Color theory perception of steady wide band liquid crystal thermometry. Exp Therm Fluid Sci 39:112–122
28. Kline SJ, McClintock FA (1953) Describing uncertainties in single sample experiments. Mech Eng 75(1):3–8
29. COMSOL Multiphysics 4.3b, Acoustics module user's guide. May 2013
30. Bauer AB (1977) Impedance theory and measurements on a porous acoustic liner. AIAA J Aircr 14(8):720–728
31. de Brederode V, Bradshaw P (1972) Three-dimensional flow in nominally two-dimensional separation bubbles: 1. Flow behind a rearward-facing step. Imperial College of Science and Technology, Dept. of Aeronautics, London
32. Cukurel B, Selcan C, Arts T (2013) Film cooling extraction effects on the aero-thermal performance of rib roughened cooling channel flow. ASME J Turbomach 135(2):021016-1–021016-12
33. Cukurel B, Arts T (2013) Local heat transfer dependency on thermal boundary condition in ribbed cooling channel geometries. J Heat Transf-Trans ASME 135(10):101001-1–101001-11